Chemical Science

ROYAL SOCIETY OF CHEMISTRY

EDGE ARTICLE

View Article Online
View Journal | View Issue

Cite this: *Chem. Sci.*, 2024, **15**, 7689

All publication charges for this article have been paid for by the Royal Society of Chemistry

Received 12th March 2024
Accepted 16th April 2024

DOI: 10.1039/d4sc01696c

rsc.li/chemical-science

Amorphous conversion in pyrolytic symmetric trinuclear nickel clusters trigger trifunctional electrocatalysts†

Li Li,[a] Hui-Feng Zhao,[a] Mei-Xing Gan,[b] Tao Zhang,[a] Jia-Ning Li,[b] Shi Tao,*[c] Jing Peng,[d] Hai-Bin Yu *[a] and Xu Peng *[b]

The pursuit of multifunctional electrocatalysts holds significant importance due to their comprehension of material chemistry. Amorphous materials are particularly appealing, yet they pose challenges in terms of rational design due to their structural disorder and thermal instability. Herein, we propose a strategy that entails the tandem (low-temperature/250–350 °C) pyrolysis of molecular clusters, enabling preservation of the local short-range structures of the precursor Schiff base nickel ($Ni_3[2(C_{21}H_{24}N_3Ni_{1.5}O_6)]$). The temperature-dependent residuals demonstrate exceptional activity and stability for at least three distinct electrocatalytic processes, including the oxygen evolution reaction (η_{10} = 197 mV), urea oxidation reaction (η_{10} = 1.339 V), and methanol oxidation reaction (1358 mA cm^{-2} at 0.56 V). Three distinct nickel atom motifs are discovered for three efficient electrocatalytic reactions (Ni1 and Ni1′ are preferred for UOR/MOR, while Ni2 is preferred for OER). Our discoveries pave the way for the potential development of multifunctional electrocatalysts through disordered engineering in molecular clusters under tandem pyrolysis.

Introduction

Developing clean and renewable energy sources to address the energy crisis has attracted worldwide interest. In the era of next-generation energy, water splitting for hydrogen production and fuel cell applications has garnered a lot of attention.[1] Overall water splitting requires the oxygen evolution reaction (OER),[2] while fuel cells necessitate the urea oxidation reaction (UOR)[3] and methanol oxidation reaction (MOR).[4] Multifunctional electrocatalysts are materials that can efficiently catalyze multiple electrochemical reactions, such as OER, UOR and MOR.[5] These electrocatalysts are important for various technologies, such as fuel cells,[6] electrolyzers,[7] and metal–air batteries,[8] as they can improve the overall performance and efficiency of these devices. Importantly, multifunctional electrocatalysts can enable the development of integrated systems that perform multiple electrochemical reactions in a single device, leading to more compact and efficient energy conversion systems.[9]

The design and synthesis of efficient and stable multifunctional electrocatalysts present significant challenges. This is because those different electrochemical reactions take place *via* different mechanisms. The OER comprises four-electron transfer steps, resulting in the evolution of O_2. In contrast, the UOR proceeds through six-electron transfer steps, converting urea into CO_2 and N_2. The mechanism of the MOR is more complex, involving six-electron transfers. Therefore, designing a multifunctional catalyst for OER, UOR, and MOR that simultaneously meets criteria for uniformity, efficiency, and stability is a challenge.[10–12]

Amorphous materials are characterized by long-range disorder and only short-range order.[13,14] Their local atomic environment and electronic states can be modulated to enhance the intrinsic reactivity of each site, meeting the requirements of multifunctional catalysts. The abundant defects and inherent structural disorder greatly facilitate charge transfer and ion diffusion.[15] Therefore, they possess more abundant active sites, wider compositional ranges, and higher structural flexibility.[16] However, the design of amorphous materials poses challenges because of their disordered and unstable structures. Currently, there is no universal approach that can effectively control highly efficient structures. The

[a]*Wuhan National High Magnetic Field Center, School of Physic, Huazhong University of Science and Technology, Wuhan 430074, China. E-mail: haibinyu@hust.edu.cn*

[b]*College of Chemistry and Chemical Engineering, Hubei University, Wuhan 430062, China. E-mail: pengxu@hubu.edu.cn*

[c]*School of Electronic and Information Engineering, Jiangsu Laboratory of Advanced Functional Materials, Changshu Institute of Technology, Changshu 215500, China. E-mail: taoshi@cslg.edu.cn*

[d]*Shenzhen Key Laboratory of Energy Materials for Carbon Neutrality, Shenzhen Institutes of Advanced Technology, Chinese Academy of Sciences, Shenzhen 518055, China*

† Electronic supplementary information (ESI) available. CCDC 2270095. For ESI and crystallographic data in CIF or other electronic format see DOI: https://doi.org/10.1039/d4sc01696c

intrinsic correlation between structure and activity remains unclear.[17,18]

To study the detailed or characteristic structure of amorphous materials, scientists often study their transition from crystalline to amorphous. By studying the degree and the path of amorphous change, along with modulating defects or disorders in crystals, structural insights into amorphous materials can be obtained. Based on the above theory, our experience of the effect of pyrolysis on coordination molecular clusters can play a good demonstration role.[19,20] We have studied the process of coordination of molecular clusters from crystalline to amorphous and later to crystalline during pyrolysis and determined the *in situ* reconstruction process and information about the amorphous structure.[21] However, previous studies often focused on the stage of high-temperature pyrolysis transformation (above 400 °C), where the structure is easy to characterize and clear in crystalline materials. The transformation mechanism of tandem pyrolysis (low temperature <400 °C) in amorphous materials has not been well studied, and the difficulty of research is greater due to the lower degree of amorphous material.

Therefore, it is crucial to design a tandem pyrolysis system with clear crystalline and amorphous transition processes to clarify the electrochemical performance changes and active site selectivity design of electrocatalysts during crystalline and amorphous transition processes. Herein, we propose a tandem pyrolysis approach that retains partial local coordination environments of the crystalline phase, providing the possibility of highly dispersed active sites. Controlling amorphous structures through tandem pyrolysis triggers a chemical environment of metals in the crystalline phase that can be retained, unlike high-temperature pyrolysis of organic frameworks, which causes structural collapse due to traditional carbon graphitization. Surprisingly, obtained disordered materials from symmetric trinuclear nickel clusters exhibit three excellent electrocatalytic functionalities (OER/UOR/MOR) with distinct selectivity, Ni1, Ni1′ and Ni2, where this paves the way for potentially developing multifunctional electrocatalysts through disordered engineering and provides insights into establishing structure–property relationships in amorphous materials.

Results and discussions

The schematic illustration of tandem pyrolysis in Ni_3 crystal was shown in Scheme 1. The single-crystal X-ray diffraction data found Ni_3 belongs to the triclinic crystal system $P\bar{1}$ space group. The nickel (Ni) atoms are coordinated by two O bridges in an opposing direction, with Ni1 and Ni1′ being connected to Ni2 *via* μ2-O1 and μ2-O1′ bridge connections, two O bridges in opposite directions, Ni atoms are chelated by N on the ligand imine and O on the phenolic hydroxyl group. The oxygen on the free hydroxyl group on the ligand and O on the DMF molecule are not involved in the coordination (Fig. S2†). The bond lengths of Ni1–N1 and Ni1–N2 in the compound are 2.012 (4) Å and 2.026 (4) Å, respectively. The bond lengths of Ni1–O1, Ni1–O2, and Ni1–O5 in the compound are 1.997 (3) Å, 2.029 (3) Å, and 2.215 (3) Å, respectively.

The TG curve is shown in Fig. 1a, mass losses and corresponding temperatures during the three stages of pyrolysis are 3.33%, 22.6%, and 21.74%, respectively. The pyrolysis process

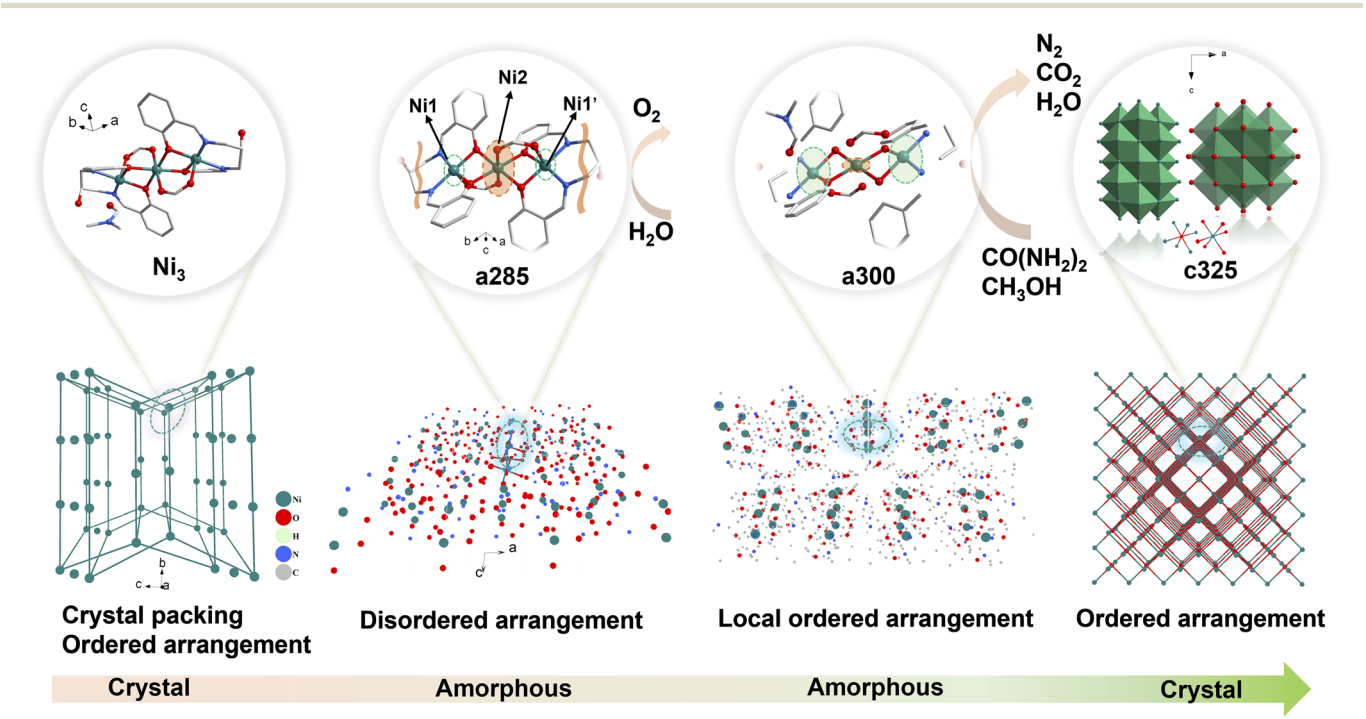

Scheme 1 Schematic illustration of the crystal transformation *via* tandem pyrolysis. Schematic diagram depicts the tandem pyrolysis induced transformation of crystalline Ni_3 into amorphous a285, and its subsequent high-temperature pyrolysis reconstruction into a crystalline structure. The transformation process is monitored by TG-MS, which detects the overflow of organic small molecule fragments during pyrolysis.

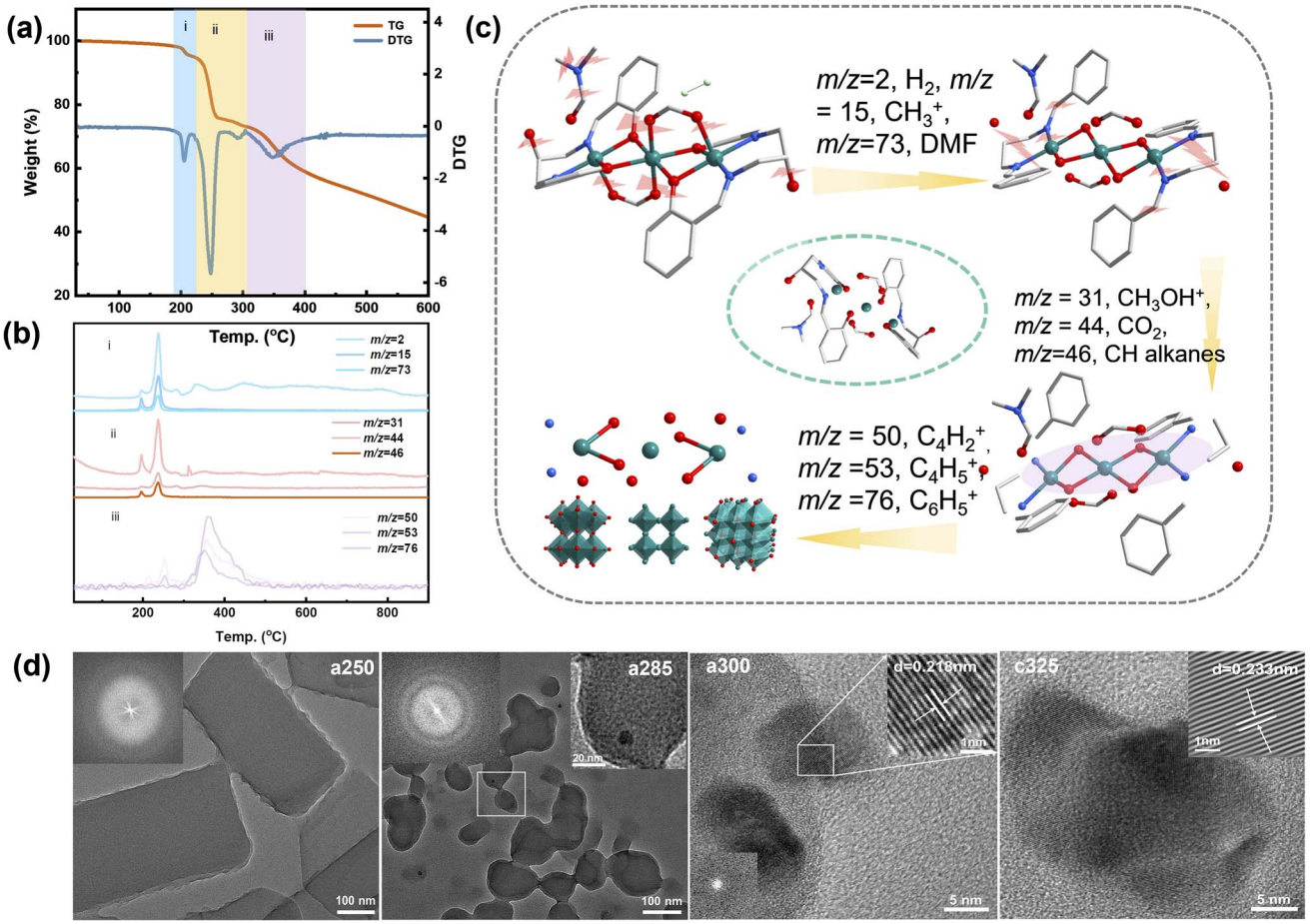

Fig. 1 Tracking structural evolution in tandem pyrolysis to uncover the mechanism of amorphous and crystalline transformation products. (a) TG and DTG curves of Ni_3; (b and c) TG-MS curves of organic fragments from decomposition products $m/z = 2$, H_2; $m/z = 15$, CH_3^+; $m/z = 73$, DMF; $m/z = 31$, CH_2CHOH^+; $m/z = 44$, CO_2; $m/z = 46$, $CH_2CHOHCH_2^+$; $m/z = 50$, $C_4H_2^+$; $m/z = 53$, $C_4H_5^+$; $m/z = 76$, $C_6H_5^+$ derived from Ni_3. (d) HRTEM images of a250, a285, a300 and c325; the inset is the Fourier transform, showing lattice stripes.

of the compounds is divided mainly into three stages: (i) the first stage is the loss of guest molecules at 213 °C and the main source of H_2 ($m/z = 2$, where hydrogen is obtained from the condensation of aromatic structures), CH_3^+ ($m/z = 15$), and DMF ($m/z = 73$). (ii) The second stage at 213–308 °C is the basic pyrolysis stage of the complex, and the main small molecular fragments lost include CH_2CHOH^+ ($m/z = 31$), CO_2 ($m/z = 44$), $CH_2CHOHCH_2^+$ ($m/z = 46$). (iii) The third stage starts at 310 °C and lasts until 900 °C. There is a rapid weight loss stage between 308 °C and 413 °C, accompanied by the loss of $C_4H_2^+$ ($m/z = 50$), $C_4H_5^+$ ($m/z = 53$) and $C_6H_5^+$ ($m/z = 76$). According to TG-MS data (Fig. 1b and c), following chemical reactions occurred in this process:

$$2C_{21}H_{24}N_3Ni_{1.5}O_6 \rightarrow C_xH_{x-1}N_yNi_{y/2}O_z + H_2, \text{DMF} + \text{chain alkanes} \quad (1)$$

$$C_xH_{x-1}N_yNi_{y/2}O_z \rightarrow \text{hydrocarbons } (C_xH_{x-1}CHOHCH) + \text{N-containing, C hybrid compounds} + \text{amorphous state } NiO_x \quad (2)$$

$$\text{Hydrocarbons } (C_xH_{x-1}CHOHCH) \rightarrow Ni/NiO_x@NCs \quad (3)$$

$$2C_{21}H_{24}N_3Ni_{1.5}O_6 \rightarrow \text{amorphous state } NiO_x \rightarrow Ni/NiO_x@NCs \quad (4)$$

Scanning and transmission electron microscopy (SEM and TEM) were utilized to examine the morphology, size, and microstructure of pyrolysis products. The sample subjected to tandem-temperature pyrolysis exhibited an amorphous structure, as evidenced by diffuse rings in fast Fourier transform (FFT) patterns and high-resolution TEM (HRTEM) images (Fig. 1). a250 and a285 samples were confirmed to be amorphous by TEM analysis of heat-treated samples (Fig. 1d). The corresponding FFT patterns (insets of Fig. 1d) displayed a diffuse ring for the edge and a halo pattern for the core, further corroborating the amorphization in the edge region.[22] After collapse of the structure, c325 particles agglomerated, but no obvious difference was observed in the microscopic morphology before and after agglomeration (Fig. S4†). This indicates that the sample tends towards stability.[23] Further analysis verified that main products after pyrolysis were Ni and NiO, along with a peripheral carbon layer. Due to the uniform

distribution of metal, oxide, and carbon layers, the nickel metal is largely exposed, which may facilitate faster electron transfer for improved electrocatalytic performance.[24]

The representative peaks at 44.5°, 51.8°, and 76.4° are assigned to (111), (200), and (220) planes of metallic nickel (JCPDS 04-0850),[25] respectively, indicating the amorphous nature of c325. When the pyrolysis temperature reaches 250 °C, the crystal structure has changed, and wide peaks appear at about $2\theta = 8.59°$ for a285 and a300, which proves that the compound has changed from a crystalline state to an amorphous and crystalline transition state (Fig. 3a). Compared with the Ni/NiO standard card, the crystal plane index of c325 contains mainly NiO (JCPDS 47-1049)[26] and Ni (JCPDS 04-0850) after pyrolysis at 325 °C.

The surface chemical states of a250, a285, a300, and c325 were examined by XPS. The surface chemical composition consisted of C, N, O, and Ni (Fig. 2b). The high-resolution Ni 2p spectrum displayed a peak at 855.8 eV for Ni $2p_{3/2}$ of Ni^{3+}, along with two satellite peaks at 862.3 eV and 880.6 eV, indicating the oxidation of surface Ni to Ni(II) or Ni(III) in the pyrolysis products. Compared to standard XPS data for nickel compounds, the peak positions of the c325 samples at 856.8 eV (Ni $2p_{3/2}$) and 874.3 eV (Ni $2p_{1/2}$) exhibited a positive shift *versus* standard NiO positions, while typical NiO satellite peaks were at 860.6 eV and 877.9 eV; the two satellite peaks of pyrolysis samples (862.3 eV and 880.6 eV) shifted forward, suggesting that the surface Ni existed predominantly as Ni(III). The literature standard peak positions for Ni(III) in NiO_x were 855.5 eV (Ni $2p_{3/2}$) and 873.3 eV (Ni $2p_{1/2}$).[27] Compared to standard positions, the peak positions of synthesized samples were positively shifted (Fig. 2c), indicating that the nickel valence state on the surface of our prepared samples was higher than the typical Ni(III). Since high-valent nickel serves as active sites for methanol adsorption, this may promote high activity for the methanol oxidation reaction.[28]

Using PDF analyses, more information on the structure and particle size of Ni species can be obtained. The small crystallite sizes cause deviations on the absolute scale for $G(r)$ and intensity ratios. At short range (below γ of 10 Å, Fig. 2d), both PDFs are practically equal, not only in the position of the peaks but also in their intensity. The peaks at 2.48 Å, 3.52 Å, 4.30 Å, 5.56 Å, and 6.56 Å belong to Ni^0. 3.01 Å, 5.10 Å, and 6.61 Å, which correspond to Ni–O, are consistent with XANES results. X-ray absorption near-edge structure (XANES) and extended X-ray absorption fine structure (EXAFS) spectroscopy analyses were conducted. The XANES spectrum at the Ni K-edge revealed that compound Ni_3 exhibited the highest white line intensity, whereas the Ni foil displayed the lowest intensity.[29]

The experimental findings indicate that at 285 °C, the nickel (Ni) valence state lies between Ni^{2+} and Ni^{3+} (Fig. 2e). After tandem pyrolysis, the Ni valence state in each sample exceeds that of the initial sample. Notably, in the a250 sample, the Ni valence state remains lower than the original, implying retention of its metallic phase during pyrolysis. The reciprocal space (R-space) analysis reveals two distinct coordination peaks at 1.61 and 2.15 Å (uncorrected for phase shift) (Fig. 2f), assignable to Ni–O/N and Ni–Ni interactions, respectively. Specifically, a285 predominantly exhibits the Ni–O/Ni–N form, with the 2.15 Å peak corresponding to the single scattering path of Ni–Ni.

The spectral analysis of a300 closely resembles that of nickel, maintaining stability at approximately 2.15 Å. For a250, a285, a300, and c325, dual peaks in the EXAFS spectrum are evident, appearing at 1.73 Å and 2.14 Å, respectively. Focusing on Fourier-transformed (FT) peaks near 1.73 Å, a detailed analysis reveals an average Ni–Ni spacing marginally shorter than that of Ni^{3+} (2.49 Å), indicating the presence of coordination unsaturation and structural distortion in the local coordination of nickel (Ni–O or Ni–N).[30] Concomitantly, close to 2.14 Å, the FT peak resulting from the single scattering of the Ni–Ni path suggests the existence of metallic phases. The observable strength of the Ni–Ni bond peak in a300 and Ni–O coordination in c325 imply that 300 °C represents a temperature node for the structural transition from an amorphous to a crystalline state. This structural insight underscores the complex interplay between tandem pyrolysis and evolution of nickel coordination environments in examined samples.[31]

The catalytic performance of prepared electrocatalysts is evaluated by electrochemical testing, and the OER conversion mechanism is as follows:[5]

$$Ni + 2OH^- \rightarrow Ni\text{–}O + H_2O + 2e^-$$

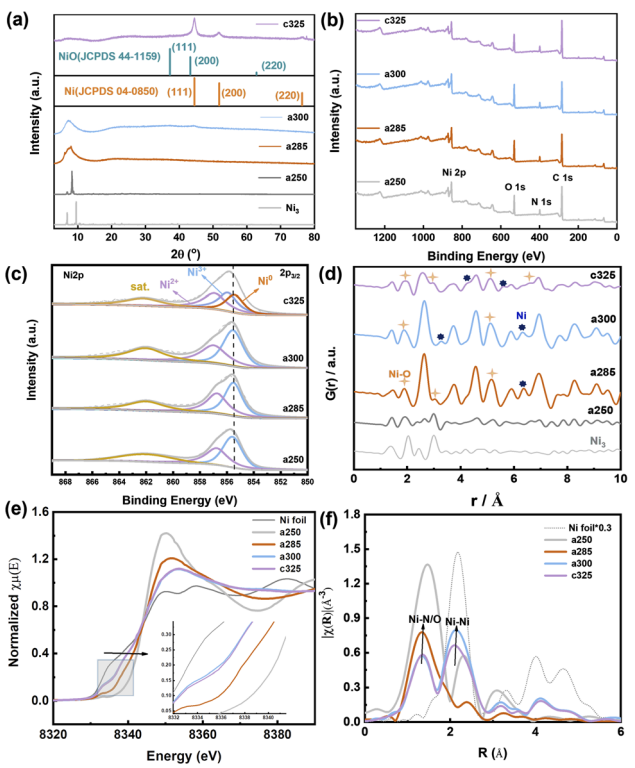

Fig. 2 Physical property and chemical bonding environment analysis. (a) XRD patterns of Ni_3, a285, a300, and c325 at $2\theta = 3$–80. (b) XPS spectra of a250, a285, a300 and c325. (c) Ni $2p_{3/2}$. (d) Atomic pair distribution function (PDF) for a250, a285, a300 and c325. (e) *In situ* Ni K-edge XANES spectra of a250, a285, a300 and c325, the inserted picture is a magnification of XANES spectra in the region. (f) Fourier transform (FT) curves and Ni K-edge EXAFS spectra of Ni_3.

$$Ni–O + 2OH^- \rightarrow Ni + O_2 + 2H_2O + 2e^-$$

$$UOR: Ni + OH^- \rightarrow Ni–OH$$

$$6Ni(OH)_2 + 6OH^- \rightarrow 6NiOOH + 6H_2O + 6e^- + CO(NH_2)_2 \rightarrow 6Ni(OH)_2 + N_2 + CO_2(g).$$

$$MOR: Ni + OH^- \rightarrow Ni–OH$$

$$Ni–CH_3OH^* \rightarrow OH^–CH_3O^* \rightarrow CH_2O^* \rightarrow CHO^* \rightarrow CO^* \rightarrow COOH^* \rightarrow CO_2 + H_2O.$$

Due to the pronounced electronic correlation effect within the three-dimensional orbitals of nickel atoms, catalysts based on nickel have consistently been a focal point in OER research. The redox peak of Ni(II)/Ni(III) is susceptible to oxidation, showcasing the potential of nickel-based materials for finely tuning electronic structures and serving as effective active sites for methanol oxidation. This insight prompted an investigation into the electrocatalytic performance of OER/UOR/MOR under alkaline conditions. The electrocatalytic OER performance of all catalysts (a250, a285, a300, and c325) was assessed *via* LSV using a standard three-electrode system in a nitrogen-saturated 1 M KOH electrolyte. In Fig. 3a, a285 exhibited a mere 197 mV overpotential to achieve a reference current density of 10 mA cm^{-2}. Tafel plots, derived from polarization curves to gain deeper insight into electrochemical reaction kinetics (Fig. S9†), revealed a Tafel slope of 156.21 mV dec^{-1} for a285 and 161.44 mV dec^{-1} for a300.

The data demonstrates that a285 and a300 also exhibit good dynamics at high current densities of 50 mA cm^{-2}. Fig. 3b illustrates the equivalent circuit diagram used for fitting, where R_s represents the contact resistance, which can be respectively represented as charge transfer resistance (R_{ct}) and Warburg impedance (Z_w), with R being the internal resistance,[32] the value of the X-axis intercept of the semicircle, which was 4.30 Ω cm^2 before the first cyclic voltammetry cycle. The Faraday process can be further divided into two parts: charge transfer and mass transfer.[33] The Nyquist plot shows that a285 has the smallest semicircle radius, indicating the minimum charge transfer resistance (R_{ct}). This could be attributed to the rapid reaction kinetics of electrocatalytic water oxidation or the large specific surface area.[34] We quantified the electrochemically active surface area (ECSA) through electrochemical double-layer capacitors (C_{dl}). CV curves in the non-Faraday region, recorded at various scanning rates (20, 40, 60, 80, and 120 mV s^{-1}) in 1.0 M KOH, are presented. The C_{dl} of a300 was determined to be 12.00 mF cm^{-2} by calculating the difference in current density at half of the slope using the linear relationship $(j_a - j_c)/2$. Following closely, the C_{dl} value of a285 was measured as 8.72 mF cm^{-2} (Fig. S10†).

Recognizing the long-term durability as a pivotal indicator in the development of high-performance electrocatalysts, these findings contribute to a comprehensive assessment of electrochemical characteristics and potential applications of studied materials.[35] The stability of a285 was evaluated through chronoamperometry in 1.0 M KOH at a constant overpotential of 50 mV, as depicted in Fig. 3c. Following more than 24 hours of long-term stability testing, the potential required to maintain current density exhibited minimal variation. Subsequent to stability testing, LSV was conducted again, the overpotential was measured as 260 mV at 10 mA cm^{-2}, underscoring the excellent stability of the a285 sample in long-term oxygen evolution reactions under alkaline conditions.

We normalized the current density based on the corresponding roughness factor (R_f) obtained from ECSA results (Fig. 3d). At a 350 mV overpotential, the specific current density of a300 was 0.04 mA cm^{-2}, while that of a285 was 0.06 mA cm^{-2}. The higher specific current density of a285 compared to the control sample a300 suggests that a285 is inherently more active. This phenomenon may arise from the synergistic effect of exposing more active sites in unique structural features of a285, along with the accelerated electron transfer and significantly improved OER activity induced by Ni^{3+} species on the oxidation surface.

The UOR performance was evaluated in oxygen-saturated 1 M KOH + 0.33 M urea. For a300, a sharp increase in the anodic current was observed at an onset potential of 1.339 V *vs.* RHE. The electrode potentials at 10 mA cm^{-2} were 1.355 V, 1.347 V, and 1.339 V for a250, a285, and a300 electrodes, respectively. The Tafel slope of a300 was as low as 10.15 mV dec^{-1}, lower than a285 (12.65 mV dec^{-1}) or c325 (20.59 mV dec^{-1}) (Fig. 4a). This indicates that the reaction follows the Volmer-Tafel mechanism where the chemical recombination of adsorbed H is the rate-determining step. The low Tafel slope of a300 signifies high UOR catalytic activity arising from fast and efficient charge and mass transfer during the catalytic process.[36]

In Fig. 4b, the electrochemical impedance spectrum of the catalyst after the addition of urea solution reveals that the a300 catalyst exhibits the optimal kinetic process. The

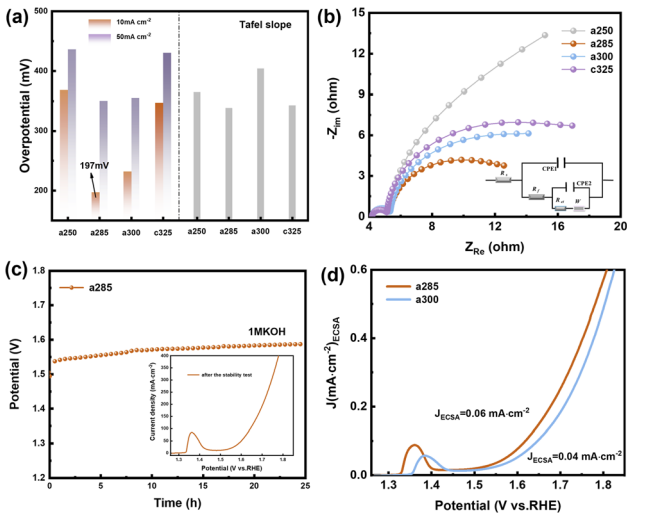

Fig. 3 Oxygen evolution reaction (OER) catalytic performance. (a) Overpotentials at typical current densities and comparison of Tafel slopes. (b) EIS plots. (c) Durability test at 1.2 and 1.8 V *vs.* RHE for 25 h of a285. LSV curve after time stability test. (d) Normalized LSV curve of current density.

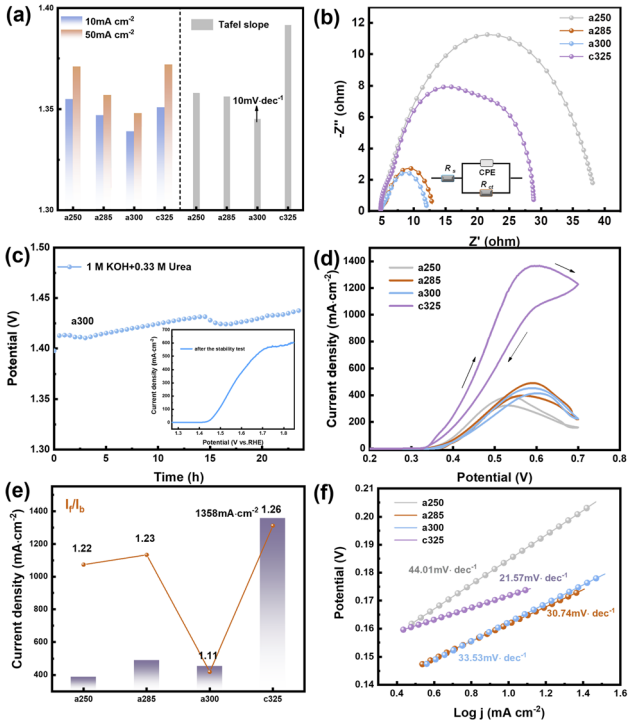

Fig. 4 UOR and MOR catalytic performance. (a) Potential and Tafel slope of the four catalysts at 10 and 50 mA cm^{-2} in 1.0 M KOH + 0.33 M urea. (b) EIS curves and equivalent circuit of the electrocatalysts. (c) Long-term stability evaluation of a300 at 10 mA cm^{-2} using the chronoamperometry method. (d) CV curves at 50 mV s^{-1} in 1 M KOH + 0.5 M methanol. (e) Ratio of forward peak (I_f) to reverse peak (I_b) during forward scanning. (f) Tafel slope fitted according to the d-plot curve.

electrochemical double-layer capacitance fitting curve, derived from the cyclic voltammetry curve within the valid Ladi interval (Fig. S15†), confirms that the a300 sample possesses the highest C_{dl} value (C_{dl} = 2.31 mF cm^{-2}), indicative of a relatively large electrochemical specific surface area. Utilizing eqn (4), turnover frequency (TOF) values for the catalyst were calculated as 0.22 s^{-1}, 0.26 s^{-1}, 0.11 s^{-1}, and 0.16 s^{-1}, respectively. The a300 catalyst demonstrates robust intrinsic activity. In Fig. 4c, the chronopotentiometric curve of a300 over 24 hours reveals sustained performance, and subsequent LSV curve scanning indicates a rise in potential and a decrease in the number of active sites. This decline in active sites, coupled with the extended sample consumption over time, suggests that the favorable UOR response is likely to be attributable to the presence of abundant active sites in the catalyst.

The MOR performance of the pyrolysis electrocatalyst was assessed through CV in 1.0 M KOH and 0.5 M methanol solution. Prior to MOR testing, a CV activation consisting of 50 cycles was conducted in a solution of 1 M KOH and 0.5 M CH_3OH until a stable curve shape was achieved. The resulting CV curve exhibits two distinct oxidation peaks, with the forward peak current (I_f) during forward scanning and reverse peak current (I_b) during reverse scanning occurring around 0.55 V. I_f is associated with the formation of intermediate product CO during methanol oxidation, while I_b corresponds primarily to the oxidation of adsorbed intermediate species that are not fully oxidized.[37] The peak current density of c325 is notably the highest at 1358 mA cm^{-2}, surpassing that of a250 (388 mA cm^{-2}), a285 (490 mA cm^{-2}), and a300 (453 mA cm^{-2}) (Fig. 4d). This performance is superior to that of most reported Ni-based electrocatalysts, underscoring the efficacy of c325 in methanol oxidation reactions.

The Tafel slopes for methanol electrooxidation of a250, a285, a300, and c325 were 44.01, 30.74, 33.53, and 21.57 mV dec^{-1}, respectively (Fig. 4f). Compared to other groups, c325 exhibited the lowest Tafel slope, indicating significantly enhanced kinetics for methanol electrooxidation. Key indicators of electrocatalytic efficiency and catalyst tolerance to carbonaceous intermediates are I_f and I_b values.[38] The I_f/I_b ratios were 1.22, 1.23, 1.11, and 1.26 for a250, a285, a300, and c325, respectively (Fig. 4e). This improved electrooxidation performance is attributed primarily to abundant nickel active sites and unsaturated coordination in the amorphous material continually generated by decomposition of the complex framework.[39] The c325 sample exhibited a C_{dl} of 2.4 mF cm^{-2} (Fig. S16†), indicating a large electrochemically active surface area. The fracturing of the peripheral carbon skeleton and formation of N–Ni, Ni–O, and Ni–Ni bonds likely exposed more Ni nanocrystals, increasing the specific surface area and MOR activity. Based on electrochemical results, we demonstrate the tremendous potential of amorphous and crystalline derivatives prepared from Ni_3-derived precursors for OER, UOR and MOR electrocatalytic applications.[40]

DFT calculations were performed to elucidate the underlying mechanism for the enhanced OER performance. Ni sites play an important role in the catalytic process, as the density of states (DOS) of the Ni2 atom in Ni_3 crystals and a285 is concentrated at the Fermi level. Adsorption of electrons on the Ni2 surface can shift the d-band center of the Ni2 atom in a285 closer to the Fermi level (Fig. 5b). The higher OER activity could be attributed to stabilized OH^- adsorption on the Ni2 surface, which accelerates O_2 evolution (Fig. 5d). The remarkable OER electrocatalytic activity and stability of a285 can be ascribed to

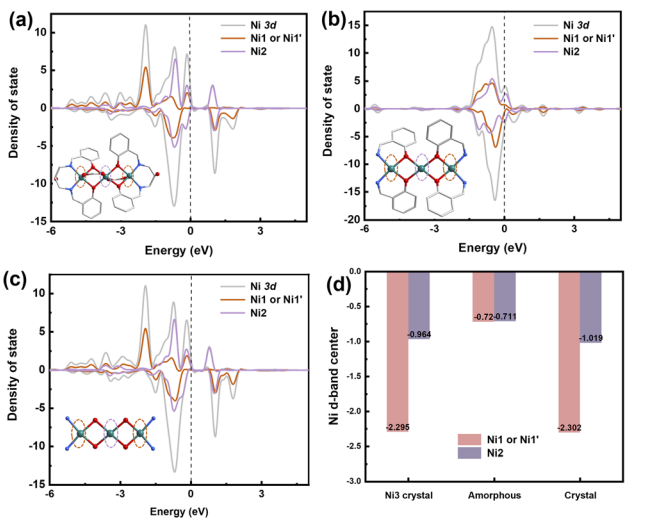

Fig. 5 Theoretical calculation. (a) Density of states (DOS) (N 2p) of (a) Ni_3-crystal, (b) a285, and (c) c325 crystal. (d) D-band of nickel atoms.

following reasons. As demonstrated by combined TG-MS, XPS, XANES, and DFT analyses, the amorphous structure provides rich 3d diffusion channels for charge carriers and contains highly dispersed Ni2 sites with defined charge states and bonding. This enables selective and efficient catalysis of specific reactions. The outstanding electrocatalytic performance of a285 further validates the structural advantages of the nickel complex.

Conclusions

In summary, we have uncovered modulation mechanisms of electrocatalytic oxygen/urea/methanol oxidation reactivity correlated with crystalline-to-amorphous transitional motifs in nickel clusters mediated by prudent tandem-temperature pyrolysis through rigorous experimentation combined with theoretical calculations. *In situ* TG-MS technology coupled with X-ray distribution function analysis was utilized to investigate the crystalline-to-amorphous transformation of Ni_3 during tandem pyrolysis. A homogeneous amorphous material was generated in the pyrolysis process, primarily attributed to inadequate ligand fracturing, which facilitated electron transfer. Density functional theory calculations further revealed that the three amorphous Ni atoms were located near the Fermi level. The Ni2, Ni1 and Ni1′ components not only offer abundant diffusion pathways for hydroxyl ions but also possess highly dispersed nickel metallic sites, a concentrated density of states, and definitive interfacial bonding. Moreover, Ni2, Ni1 and Ni1′ nanoparticles catalyze oxygen evolution reactions (a285) and urea (a300)/methanol (c325) oxidation reactions with remarkably high selectivity and efficiency (η_{10} = 197 mV, η_{10} = 1.339 V and 1358 mA cm^{-2} at 0.56 V, respectively). Such attributes render this material among the most exceptional nickel-based electrocatalysts for these reaction systems, unveiling new opportunities to enable enhanced oxygen evolution through electronic structure engineering of nickel metal (or amorphous compounds) for water splitting applications.

Data availability

All experimental data associated with this article have been included in the main text and ESI.†

Author contributions

Xu Peng and Hai-Bin Yu conceived the idea, co-wrote the paper and supervised the whole experimental procedure and data analysis. Li Li, Hui-Feng Zhao, Mei-Xing Gan, Tao Zhang, Jia-Ning Li, Shi Tao and Jing Peng performed the experiments, analyzed the data and wrote the manuscript. All the authors discussed the results, commented on and revised the manuscript.

Conflicts of interest

There are no conflicts to declare.

Acknowledgements

This work is supported by the National Thousand a Young Talents Program of China, Fundamental Research Funds for the Central Universities (2018KFYXKJC009), Wuhan Knowledge Innovation Special Project (2023020201020422), and Natural Science Foundation of the Jiangsu Higher Education Institutions (23KJA430001).

Notes and references

1 N. K. Oh, J. Seo, S. Lee, H. J. Kim, U. Kim, J. Lee, Y. K. Han and H. Park, Highly efficient and robust noble-metal free bifunctional water electrolysis catalyst achieved via complementary charge transfer, *Nat. Commun.*, 2021, **12**, 4606.

2 R. Zhang, W. Liu, F.-M. Zhang, Z.-D. Yang, G. Zhang and X. C. Zeng, COF-C4N Nanosheets with uniformly anchored single metal sites for electrocatalytic OER: from theoretical screening to target synthesis, *Appl. Catal., B*, 2023, **325**, 122366.

3 S. Xu, X. Ruan, M. Ganesan, J. Wu, S. K. Ravi and X. Cui, Transition Metal-Based Catalysts for Urea Oxidation Reaction (UOR): Catalyst Design Strategies, Applications, and Future Perspectives, *Adv. Funct. Mater.*, 2024, 2313309.

4 H. Cheng, B. Dong, Q. Liu and F. Wang, Direct Electrocatalytic Methanol Oxidation on MoO3/Ni(OH)2: Exploiting Synergetic Effect of Adjacent Mo and Ni, *J. Am. Chem. Soc.*, 2023, **145**, 26858–26862.

5 M. Hao, J. Chen, J. Chen, K. Wang, J. Wang, F. Lei, P. Hao, X. Sun, J. Xie and B. Tang, Lattice-disordered high-entropy metal hydroxide nanosheets as efficient precatalysts for bifunctional electro-oxidation, *J. Colloid Interface Sci.*, 2023, **642**, 41–52.

6 Y. Li, L. Zhao, X. Du, W. Gao, C. Zhang, H. Chen, X. He, C. Wang and Z. Mao, Cobalt-doped IrRu bifunctional nanocrystals for reversal-tolerant anodes in proton-exchange membrane fuel cells, *Chem. Eng. J.*, 2023, **461**, 141823.

7 X. Zhang, A. Wu, D. Wang, Y. Jiao, H. Yan, C. Jin, Y. Xie and C. Tian, Fine-tune the electronic structure in Co-Mo based catalysts to give easily coupled HER and OER catalysts for effective water splitting, *Appl. Catal., B*, 2023, **328**, 122474.

8 P. Thangavel, H. Lee, T.-H. Kong, S. Kwon, A. Tayyebi, J.-h. Lee, S. M. Choi and Y. Kwon, Immobilizing Low-Cost Metal Nitrides in Electrochemically Reconstructed Platinum Group Metal (PGM)-Free Oxy-(Hydroxides) Surface for Exceptional OER Kinetics in Anion Exchange Membrane Water Electrolysis, *Adv. Energy Mater.*, 2023, **13**, 2203401.

9 Z. Li, B. Li, M. Yu, C. Yu and P. Shen, Amorphous metallic ultrathin nanostructures: A latent ultra-high-density atomic-level catalyst for electrochemical energy conversion, *Int. J. Hydrogen Energy*, 2022, **47**, 26956–26977.

10 Z. Chen, Q. Fan, J. Zhou, X. Wang, M. Huang, H. Jiang and H. Cölfen, Toward Understanding the Formation Mechanism and OER Catalytic Mechanism of Hydroxides

by In Situ and Operando Techniques, *Angew. Chem., Int. Ed.*, 2023, **62**, e202309293.

11 A. Shahzad, F. Zulfiqar and M. Arif Nadeem, Cobalt containing bimetallic ZIFs and their derivatives as OER electrocatalysts: A critical review, *Coord. Chem. Rev.*, 2023, **477**, 214925.

12 S. Cao, J. Qi, F. Lei, Z. Wei, S. Lou, X. Yang, Y. Guo, P. Hao, J. Xie and B. Tang, Reduction-induced surface reconstruction to fabricate cobalt hydroxide/molybdenum oxide hybrid nanosheets for promoted oxygen evolution reaction, *Chem. Eng. J.*, 2021, **413**, 127540.

13 L. Zhou, P. Jiao, L. Fang, L. Liu, Z. Hao, H. Wang, Y. M. Kang, K. Zhang and J. Chen, Two-Phase Transition Induced Amorphous Metal Phosphides Enabling Rapid, Reversible Alkali-Metal Ion Storage, *ACS Nano*, 2021, **15**, 13486–13494.

14 S. Wang, W. Huo, H. Feng, Z. Xie, J. K. Shang, E. V. Formo, P. H. C. Camargo, F. Fang and J. Jiang, Enhancing Oxygen Evolution Reaction Performance in Prussian Blue Analogues: Triple-Play of Metal Exsolution, Hollow Interiors, And Anionic Regulation, *Adv. Mater.*, 2023, **35**, 2304494.

15 Z. Jia, T. Yang, L. Sun, Y. Zhao, W. Li, J. Luan, F. Lyu, L. C. Zhang, J. J. Kruzic, J. J. Kai, J. C. Huang, J. Lu and C. T. Liu, A Novel Multinary Intermetallic as an Active Electrocatalyst for Hydrogen Evolution, *Adv. Mater.*, 2020, **32**, 2000385.

16 Z. Jia, J.-L. Jiang, L. Sun, L.-C. Zhang, Q. Wang, S.-X. Liang, P. Qin, D.-F. Li, J. Lu and J. J. Kruzic, Role of Boron in Enhancing Electron Delocalization to Improve Catalytic Activity of Fe-Based Metallic Glasses for Persulfate-Based Advanced Oxidation, *ACS Appl. Mater. Interfaces*, 2020, **12**, 44789–44797.

17 J. Ding, D. Ji, Y. Yue and M. M. Smedskjaer, Amorphous Materials for Lithium-Ion and Post-Lithium-Ion Batteries, *Small*, 2024, **20**, e2304270.

18 X. Li, W. Cai, D.-S. Li, J. Xu, H. Tao and B. Liu, Amorphous alloys for electrocatalysis: the significant role of the amorphous alloy structure, *Nano Res.*, 2021, **16**, 4277–4288.

19 F. Zhou, M. Gan, D. Yan, X. Chen and X. Peng, Hydrogen-Rich Pyrolysis from Ni-Fe Heterometallic Schiff Base Centrosymmetric Cluster Facilitates NiFe Alloy for Efficient OER Electrocatalysts, *Small*, 2023, **19**, e2208276.

20 T. Li, Y. F. Wang, Z. Yin, J. Li, X. Peng and M. H. Zeng, The sequential structural transformation of a heptanuclear zinc cluster towards hierarchical porous carbon for supercapacitor applications, *Chem. Sci.*, 2022, **13**, 10786–10791.

21 L. Wang, L. Li, M. Gan, Z. Wang, T. Li, Z. Wang, Y. Li, S. Tao and X. Peng, Micro-pyrolysis perturbation promotes electrocatalytic activity of tetranuclear nickel clusters, *Electrochim. Acta*, 2023, **464**, 142794.

22 J. Liu, J. Nai, T. You, P. An, J. Zhang, G. Ma, X. Niu, C. Liang, S. Yang and L. Guo, The Flexibility of an Amorphous Cobalt Hydroxide Nanomaterial Promotes the Electrocatalysis of Oxygen Evolution Reaction, *Small*, 2018, **14**, e1703514.

23 H.-l. Li, Y.-y. Wang, C.-m. Liu, S.-m. Zhang, H.-f. Zhang and Z.-w. Zhu, Enhanced OER performance of NiFeB amorphous alloys by surface self-reconstruction, *Int. J. Hydrogen Energy*, 2022, **47**, 20718–20728.

24 S. Hu, S. Wang, C. Feng, H. Wu, J. Zhang and H. Mei, Novel MOF-Derived Nickel Nitride as High-Performance Bifunctional Electrocatalysts for Hydrogen Evolution and Urea Oxidation, *ACS Sustainable Chem. Eng.*, 2020, **8**, 7414–7422.

25 R. Yuvakkumar, S. Lee, G. W. Lee and S. I. Hong, An environment benign biomimetic synthesis of mesoporous NiO concentric stacked doughnuts architecture, *Microporous Mesoporous Mater.*, 2015, **207**, 185–194.

26 Ö. Çoban, S. Tekmen, E. Gür and S. Tüzemen, High optical response NiO, Pd/NiO and Pd/WO3 hydrogen sensors, *Int. J. Hydrogen Energy*, 2022, **47**, 25454–25464.

27 G. Chen, Z. Hu, Y. Zhu, Z.-G. Chen, Y. Zhong, H.-J. Lin, C.-T. Chen, L. H. Tjeng, W. Zhou and Z. Shao, Ultrahigh-performance tungsten-doped perovskites for the oxygen evolution reaction, *J. Mater. Chem. A*, 2018, **6**, 9854–9859.

28 M. Wang, X. Dong, Z. Meng, Z. Hu, Y. G. Lin, C. K. Peng, H. Wang, C. W. Pao, S. Ding, Y. Li, Q. Shao and X. Huang, An Efficient Interfacial Synthesis of Two-Dimensional Metal–Organic Framework Nanosheets for Electrochemical Hydrogen Peroxide Production, *Angew. Chem., Int. Ed.*, 2021, **60**, 11190–11195.

29 D. Wang, J. Wang, X. Luo, Z. Wu and L. Ye, In Situ Preparation of Mo2C Nanoparticles Embedded in Ketjenblack Carbon as Highly Efficient Electrocatalysts for Hydrogen Evolution, *ACS Sustainable Chem. Eng.*, 2017, **6**, 983–990.

30 Y. Bai, Y. Wu, X. Zhou, Y. Ye, K. Nie, J. Wang, M. Xie, Z. Zhang, Z. Liu, T. Cheng and C. Gao, Promoting nickel oxidation state transitions in single-layer NiFeB hydroxide nanosheets for efficient oxygen evolution, *Nat. Commun.*, 2022, **13**, 6094.

31 I. S. Pieta, A. Rathi, P. Pieta, R. Nowakowski, M. Hołdynski, M. Pisarek, A. Kaminska, M. B. Gawande and R. Zboril, Electrocatalytic methanol oxidation over Cu, Ni and bimetallic Cu-Ni nanoparticles supported on graphitic carbon nitride, *Appl. Catal., B*, 2019, **244**, 272–283.

32 S. S. Jeon, P. W. Kang, M. Klingenhof, H. Lee, F. Dionigi and P. Strasser, Active Surface Area and Intrinsic Catalytic Oxygen Evolution Reactivity of NiFe LDH at Reactive Electrode Potentials Using Capacitances, *ACS Catal.*, 2023, **13**, 1186–1196.

33 S. Shit, S. Chhetri, W. Jang, N. C. Murmu, H. Koo, P. Samanta and T. Kuila, Cobalt Sulfide/Nickel Sulfide Heterostructure Directly Grown on Nickel Foam: An Efficient and Durable Electrocatalyst for Overall Water Splitting Application, *ACS Appl. Mater. Interfaces*, 2018, **10**, 27712–27722.

34 S. Hu, C. Feng, S. Wang, J. Liu, H. Wu, L. Zhang and J. Zhang, Ni3N/NF as Bifunctional Catalysts for Both Hydrogen Generation and Urea Decomposition, *ACS Appl. Mater. Interfaces*, 2019, **11**, 13168–13175.

35 S. Samanta, K. Bhunia, D. Pradhan, B. Satpati and R. Srivastava, Ni and Cu ion-exchanged nanostructured mesoporous zeolite: a noble metal free, efficient, and

durable electrocatalyst for alkaline methanol oxidation reaction, *Mater. Today Energy*, 2018, **8**, 45–56.

36 B. Cui, C. Wang, S. Huang, L. He, S. Zhang, Z. Zhang and M. Du, Efficient multifunctional electrocatalyst based on 2D semiconductive bimetallic metal-organic framework toward non-Pt methanol oxidation and overall water splitting, *J. Colloid Interface Sci.*, 2020, **578**, 10–23.

37 L. Jin, Q. Meng, M. Ma, X. Gao, A. Chen, X. Sun and D. Zhou, Stable and active methanol oxidation via anchored PtRu alloy nanoparticles on NiFe layered double hydroxides, *Green Chem.*, 2024, **26**, 3221–3228.

38 R. Sha and S. Badhulika, Facile synthesis of three-dimensional platinum nanoflowers decorated reduced graphene oxide: an ultra-high performance electro-catalyst for direct methanol fuel cells, *Mater. Sci. Eng., B*, 2018, **231**, 115–120.

39 B. Habibi and N. Delnavaz, Electrooxidation of glycerol on nickel and nickel alloy (Ni–Cu and Ni–Co) nanoparticles in alkaline media, *RSC Adv.*, 2016, **6**, 31797–31806.

40 C. Wang, H. Yang, Y. Zhang and Q. Wang, NiFe Alloy Nanoparticles with hcp Crystal Structure Stimulate Superior Oxygen Evolution Reaction Electrocatalytic Activity, *Angew. Chem., Int. Ed.*, 2019, **58**, 6099–6103.